2024 International Conference on Simulation of Semiconductor Processes and Devices (SISPAD) | 979-8-3315-1635-2/24/$31.00 ©2024 IEEE | DOI: 10.1109/SISPAD62626.2024.10733296

First-Principles Calculations of Non-Equilibrium Energetics and Polarization Switching in Oxide Ferroelectric Tunnel Junctions

Kaptan Rajput
The School of Electrical Engineering
Korea Advanced Institute of Science and Technology (KAIST)
Yuseong-gu, Daejeon, Korea
kaptan@kaist.ac.kr

Ryong-Gyu Lee
The School of Electrical Engineering
Korea Advanced Institute of Science and Technology (KAIST)
Yuseong-gu, Daejeon, Korea
ronggyulee@kaist.ac.kr

Tae Hyung Kim
The School of Electrical Engineering
Korea Advanced Institute of Science and Technology (KAIST)
Yuseong-gu, Daejeon, Korea
ramanujankim@kaist.ac.kr

Hyeonwoo Yeo
The School of Electrical Engineering
Korea Advanced Institute of Science and Technology (KAIST)
Yuseong-gu, Daejeon, Korea
dndhdrnl@kaist.ac.kr

Juho Lee
The School of Electrical Engineering
Korea Advanced Institute of Science and Technology (KAIST)
Yuseong-gu, Daejeon, Korea
thinker0817@gmail.com

Yong-Hoon Kim*
The School of Electrical Engineering
Korea Advanced Institute of Science and Technology (KAIST)
Yuseong-gu, Daejeon, Korea
y.h.kim@kaist.ac.kr

***Abstract*— Ferroelectric tunnel junction (FTJ) is a promising candidate for future memory technologies and much effort has been put into the understandings of its materials and device properties. However, in view of atomistic first-principles calculations, most studies have been so far limited to the equilibrium limit and the behavior of FTJs under non-equilibrium conditions remains largely unexplored. Herein, we describe the first-principles framework that enables the analysis of FTJs under non-equilibrium conditions, which is based on the multi-space constrained-search density functional theory (MS-DFT) formalism we have developed over the years. The unique strength of MS-DFT is that the non-equilibrium free energy as well as electric field-dependent polarization and capacitance can be obtained in a first-principles manner. As an application example, for a representative $SrRuO_3$-$BaTiO_3$-$SrRuO_3$ (SRO-BTO-SRO) FTJ capacitor model, we compute the current density-voltage characteristics and tunneling electro-resistance, and the impact of polarization orientation on the resistance state.**

Keywords—Ferroelectric tunnel junctions, non-equilibrium energetics, free energy, capacitance, hysteresis profile, negative differential resistance

I. Introduction

Ferroelectric tunnel junctions (FTJs) feature a thin ferroelectric insulating layer between two metal electrodes, exhibiting switchable polarization and tunneling properties [1]. Investigating barrier profiles during polarization switching offers insights into tunnel transmission and negative capacitance, vital for memory performance and energy efficiency. To obtain the free energy profile as a function of polarization, crucial for understanding the behavior of FTJs, the standard theoretical approach has been employing equilibrium density functional theory (DFT) calculation results and fitting them to the Landau-Ginzburg-Devonshire (LGD) and Landau-Khalatnikov (LK) models [2, 3]. In addition to the important device parameters such as the critical thickness [4], interface relaxation effect [5], and mechanical load impact [6], from the first-order derivative of this free energy landscape, one can evaluate the hysteresis in the polarization vs. electric field (P-$\mathcal{E}$) and capacitance vs. electric field (C-$\mathcal{E}$) curves [7]. However, this approach is fundamentally limited in that DFT is an equilibrium theory. To address non-equilibrium energetics explicitly at the *ab initio* level, applying external electric fields to heterostructure models [8] have been proposed. However, in addition to the ambiguity in mapping voltages, the actual control parameter in experiments, to electric fields, the approach cannot be applied to asymmetric electrode cases [8]. The DFT-based non-equilibrium Green's function (NEGF) [9] approach represents a promising route to investigate the non-equilibrium electronic structure and transport properties of FTJs. However, the total energy is ill-defined within DFT-NEGF. Thus, novel methodologies are needed to achieve accurate and consistent characterizations of the energetics and device properties of FTJs.

In this study, we present the extension of the multi-space DFT (MS-DFT) formalism we have been developing over the years to ferroelectric devices, which allows the computation of non-equilibrium free energy (F-P) profile, P-$\mathcal{E}$ and C-$\mathcal{E}$ hysteresis profiles, and current density-voltage (J-V) curves.

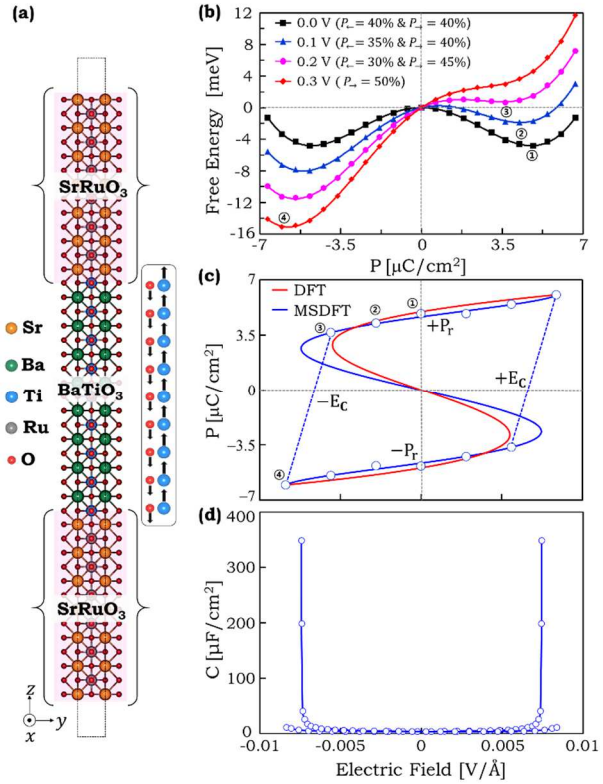

Fig. 1. (a) The representation of symmetric SRO-BTO-SRO FTJ capacitor model. **(b)** Free energy versus polarization (*F-P*) profile concerning equilibrium and finite bias is reported. **(c)** The polarization versus electric field (*P*- $\mathcal{E}$) profile computed from equilibrium DFT data (black line) and non-equilibrium MSDFT data (red line) are reported, where P_r and E_c describes the remnant polarization and coercive field. **(d)** The capacitance versus electric field (*C*- $\mathcal{E}$) profile from MSDFT data is reported. In the free energy profile, the $P_{\rightarrow}$ and $P_{\leftarrow}$ orientations quantify the degree of displacement (computed from minima of the free energy profile) from the bulk displacement values of BTO ferroelectric material. It is noted that in the free energy profile energy of paraelectric state is adopted as reference.

II. Computational Details

Model: For the considered $SrRuO_3$-$BaTiO_3$-$SrRuO_3$ (SRO-BTO-SRO) FTJ capacitor model, as illustrated in **Fig. 1(a)**, the model comprises 8 unit cells of BTO sandwiched between two electrodes, each consisting of 6 unit cells of SRO, with TiO_2 termination layers at both the interfaces. The layer stacking sequence is denoted as [SrO-$(RuO_2$-SrO$)_6$/$(TiO_2$-BaO-$TiO_2)_8$/SrO-$(RuO_2$-SrO$)_6$]. Following closely the methodology of Junquera et al. [4], we only permitted relaxation at the interfaces, while enforcing mirror symmetry within the BTO region. After obtaining the relaxed paraelectric geometry, we systematically displaced the atoms in BTO according to the displacement pattern associated with the soft modes (ξ) in bulk BTO. This process was conducted to determine the free energy profile and identify ferroelectric instability, where the strength of ξ can be evaluated from the difference in atomic displacement of BTO between ferroelectric and paraelectric phases. In order to compute the free energy profile, paraelectric state is adopted as reference.

DFT and MS-DFT calculations: An equilibrium (DFT) and non-equilibrium (MS-DFT [10-12] state calculations were conducted using the SIESTA package. The LDA functional was employed to handle exchange and correlation effects. Norm-conserving pseudopotentials based on the Troullier-Martins scheme were utilized to replace core electrons, while valence electrons were described using atomic-like orbitals at the double zeta polarized level. For Brillouin zone sampling, Monkhorst–Pack grids of 10×10×1 were employed, along with real-space mesh grid cutoff energy of 300 Ry. In the MS-DFT formalism, the top SRO, central BTO, and bottom SRO were designated as the top electrode (T), channel (c), and bottom electrode (B), respectively. The bias was controlled by the chemical potentials (μ) of the T and B electrodes, with the equation $V_b = \mu_T - \mu_B$ determining the non-equilibrium state of the channel C.

MGF calculations: Following the acquisition of the non-equilibrium electronic structure from MS-DFT, the matrix Green's function (MGF) formalism was considered for the post-processing step to obtain electron transmissions, $T(E;V) = \mathrm{Tr}[\boldsymbol{\Gamma_L G \Gamma_R G^+}]$, where the $\boldsymbol{\Gamma_{L/R}}$ is the broadening matrices and $\boldsymbol{G}$ describes the retarded Green's function for the channel region. The current density was calculated using the Landauer-Buttiker formula,

$$J(V_b) = \frac{2e}{hW}\int_{\mu_L}^{\mu_R} T(E;V_b)[f(E-\mu_R) - f(E-\mu_L)]dE \quad (1)$$

where $f(E-\mu) = 1/\{1 + exp((E-\mu)/k_BT)\}$ represents the Fermi-Dirac distribution function.

III. Results and Discussion

The computed *F-P* profile under equilibrium conditions exhibits a symmetric double-well potential, indicative of ferroelectric instability, as shown in **Fig. 1(b)**. To study the

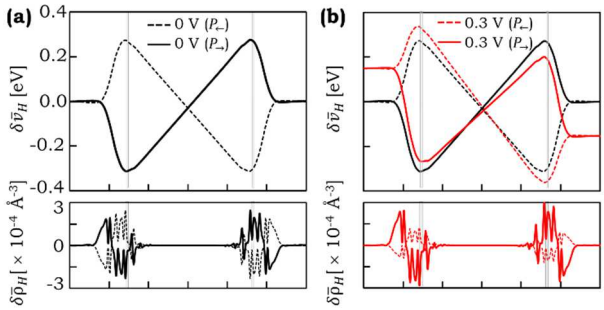

Fig. 2. (a) The difference in total electrostatic potential [$\delta\overline{v}_H = v_H^{\xi\neq0}(0) - v_H^{\xi=0}(0)$] in the top panel and the difference in total macroscopic charge density [$\delta\overline{\rho} = \rho^{\xi\neq0}(0) - \rho^{\xi=0}(0)$] in the bottom panels in equilibrium condition (difference is taken between ferroelectric state and paraelectric state) are reported. For non-equilibrium condition: **(b)** The difference in total electrostatic potential [$\delta\overline{v}_H = v^{\xi\neq0}(V) - v^{\xi=0}(0)$] and the difference in total macroscopic charge density [$\delta\overline{\rho}_H = \rho^{\xi\neq0}(V) - \rho^{\xi=0}(0)$ in top and bottom panels (difference is taken between ferroelectric state and paraelectric state) are reported. In the equations, $\xi \neq 0$ and $\xi = 0$ denote soft mode strength for polarized and non-polarized conditions, while $P_{\leftarrow}$, $P_{\rightarrow}$ and P_0 indicates the left, right ferroelectric polarization states and zero polarization paraelectric state. Shaded lines in plots represent the interfacial TiO_2 layer at left and right interfaces in paraelectric state.

non-equilibrium behavior, we applied a finite bias, observing the relative modification in the energy barrier from the free energy profile depicted in **Fig. 1(b)**. This approach allows for the identification and analysis of changes in ferroelectric properties under applied external electric fields. Given the symmetric electrode attachment in our capacitor model, applying either a positive or negative bias yields equivalent results. As the applied bias increases, the degeneracy of the free energy profile disappears. Under finite bias conditions, the energy barrier heights are modified in relation to the magnitude of the bias. The energy barrier height was measured from the energy values of the global minima corresponding to the left and right polarization states. A reduction in the energy barrier values is observed for the right polarization state, while the left polarization state shows an increase in barrier height. The threshold value for polarization switching is 0.2 V; further increases in the applied bias result in a transition from the left ferroelectric state to the right ferroelectric state. It is noted that the free energy profile depends on interface relaxation constraint, the full geometric relaxation may lead different polarization switching voltages in *F-P* profiles. From the *F-P* profile for the corresponding applied biases, we can easily obtain the *P-*$\mathcal{E}$ curve. We also compared the DFT and MSDFT hysteresis profiles. The computed values of the remnant polarizations ($\pm P_r$) and coercive field $\pm E_c$ are as $\pm$5.42 μC/cm^2 , $\pm$0.0069 V/Å, respectively. These computed values are slightly overestimated compared to the DFT (red lines) plot, indicating a clear difference between MS-DFT data from equilibrium situation. Furthermore, at the coercive field corresponding to polarization switching, we obtained the highest capacitance of 89 μF/cm^2. This can be related to the experimental observations, where the maximum capacitance is typically observed at the polarization switching voltage.

To identify the factors causing polarization switching, we analyzed the difference in total electrostatic potential and difference in macroscopic charge density profiles (difference is taken between ferroelectric state and paraelectric state), as depicted in **Fig. 2**. At equilibrium, identical dipoles near the interfaces are observed (**Fig. 1a**, bottom plot), originating from the combination of free and bound charges. The impact of applied bias on the electrostatic potential and macroscopic charge density is evident form **Fig. 2b**. The amplitude of the depolarization field can be directly inferred from the electrostatic potential profile. The slope of the macroscopic averaged electrostatic potential provides the depolarization field induced by the applied bias. For the $P_{\rightarrow}$ polarization state, the effective depolarization field increases, while for the $P_{\leftarrow}$ polarization state, it decreases. Our analysis reveals that parallel configurations of the depolarization and applied fields significantly enhance the effective depolarization field, whereas antiparallel configurations result in partial cancellation of the effective depolarization field. This is confirmed by the difference in the total electrostatic potential profile (**Fig. 2b**) corresponding to the $P_{\rightarrow}$ and $P_{\leftarrow}$ polarization states, respectively. The enhanced effective depolarization field is identified as the primary factor driving polarization switching, particularly for the $P_{\rightarrow}$ polarization state.

We analyzed the resistance state variation in regards with the $P_{\rightarrow}$ and $P_{\leftarrow}$ polarization states. Overall, higher current density were observed under positive bias conditions for $P_{\rightarrow}$ direction, as depicted in **Fig. 3(a)**. Notably, we identified the negative differential resistance (NDR) feature at 0.1 V for both polarization states. Based on our observations, we designated

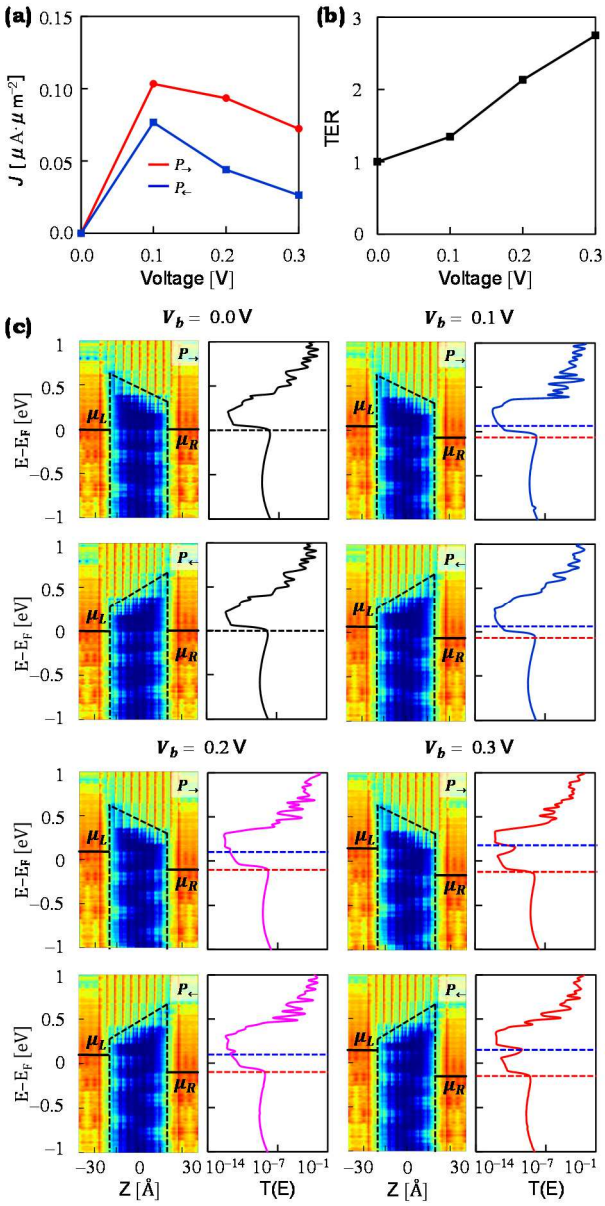

Fig. 3. (a) The current density vs. voltage (*J-V*) characteristics of symmetric FTJ model for $P_{\rightarrow}$ and $P_{\leftarrow}$ states. **(b)** Tunneling electroresistance computed from ON state and OFF state ratio. **(c)** The projected local density of state (PLDOS) (first and third column), and transmission spectra (second and fourth column) for 0.0-0.3 V are reported, respectively. In the presented PLDOS data, solid and dotted lines are used to represent the chemical potentials in the electrodes and the variations in the potential barrier height within the channel region. The dotted lines under bias conditions illustrate the relative shifts in PLDOS. Additionally, the dotted lines in the transmission graphs convey the chemical potential information, with the left and right chemical potentials denoted by red and blue colors, respectively.

the $P_{\rightarrow}$ and $P_{\leftarrow}$ polarization states as ON and OFF states, respectively. The TER was computed to be 2.75, derived from the ratio of ON and OFF states. The evaluated TER value indicate that an applied bias can effectively exhibit a noticeable TER even with symmetric electrode configurations. The partial screening of bound polarization charges at the interface results in a distorted potential profile, with the potential barrier height and asymmetric nature dependent on the polarization direction. To further analyze the distinct *J-V* behavior associated with the $P_{\rightarrow}$ and $P_{\leftarrow}$ polarization states, we examined the PLDOS (projected local density of states) and transmission spectra, as shown in **Fig. 3(c)**.

Under equilibrium conditions, the PLDOS revealed strong MIGS coupling between the left and right electrodes for both the polarization states. As the applied bias increases to 0.1 V, a significant current density increase is observed for the $P_{\rightarrow}$ polarization state. The PLDOS and transmission spectra confirm that the MIGS coupling for $P_{\rightarrow}$ polarization state is stronger than the $P_{\leftarrow}$ polarization state. Further increases in applied bias lead to the NDR feature, which corresponds to a complete decoupling of the left and right electrode MIGS states. Thus, the NDR feature is attributed to the MIGS coupling of electrodes in the FTJ.

IV. Conclusion

Utilizing a SRO-BTO-SRO FTJ capacitor model, we described a first-principles MS-DFT-based approach to analyze FTJs, which provide the *F-P*, *P-* $\mathcal{E}$, *C-* $\mathcal{E}$, and *J-V* curves. From the P-E profile, we identified the remnant polarization and coercive field. The computed free energy profile provides critical insights into polarization switching, previously unaddressed in first-principles investigations under applied bias. Through the analysis of the electrostatic potential profile, we observed a delicate balance between the applied electric field and the depolarization field necessary to sustain ferroelectricity. The I-V response revealed a NDR feature, primarily facilitated by the MIGS from the left and right electrodes. Additionally, we observed modifications in the potential barrier height relative to the applied bias. By enabling the study of FTJs in non-equilibrium states, this methodology opens new avenues for advancing memory device technology.

V. Acknowledgment

This work was supported by the National Research Foundation of Korea (2023R1A2C2003816, RS-2023-00253716).

VI. References

[1] Z. Wen and D. Wu, "Ferroelectric Tunnel Junctions: Modulations on the Potential Barrier," *Adv. Mater.,* vol. 32, no. 27, p. e1904123, Jul 2020, doi: 10.1002/adma.201904123.

[2] X. Y. Ma *et al.*, "Large family of two-dimensional ferroelectric metals discovered via machine learning," *Sci. Bull.,* vol. 66, no. 3, pp. 233-242, Feb 15 2021, doi: 10.1016/j.scib.2020.09.010.

[3] M. Zhao, G. Gou, X. Ding, and J. Sun, "An ultrathin two-dimensional vertical ferroelectric tunneling junction based on CuInP(2)S(6) monolayer," *Nanoscale,* vol. 12, no. 23, pp. 12522-12530, Jun 18 2020, doi: 10.1039/d0nr01475c.

[4] J. Junquera and P. Ghosez, "Critical thickness for ferroelectricity in perovskite ultrathin films," *Nature,* vol. 422, no. 6931, pp. 506-9, Apr 3 2003, doi: 10.1038/nature01501.

[5] G. Gerra, A. K. Tagantsev, N. Setter, and K. Parlinski, "Ionic polarizability of conductive metal oxides and critical thickness for ferroelectricity in BaTiO3," *Phys. Rev. Lett.,* vol. 96, no. 10, p. 107603, Mar 17 2006, doi: 10.1103/PhysRevLett.96.107603.

[6] X. Luo, B. Wang, and Y. Zheng, "Tunable tunneling electroresistance in ferroelectric tunnel junctions by mechanical loads," *ACS Nano,* vol. 5, no. 3, pp. 1649-56, Mar 22 2011, doi: 10.1021/nn1031438.

[7] X. Lu, H. Li, and W. Cao, "Landau expansion parameters for BaTiO3," *J. Appl. Phys.,* vol. 114, no. 22, 2013, doi: 10.1063/1.4838456.

[8] M. Stengel and N. A. Spaldin, "Ab initiotheory of metal-insulator interfaces in a finite electric field," *Phys. Rev. B,* vol. 75, no. 20, 2007, doi: 10.1103/PhysRevB.75.205121.

[9] K. Stokbro, J. Taylor, M. Brandbyge, and P. Ordejon, "TranSIESTA: a spice for molecular electronics," *Ann. N. Y. Acad. Sci.,* vol. 1006, pp. 212-26, Dec 2003, doi: 10.1196/annals.1292.014.

[10] J. Lee, H. S. Kim, and Y. H. Kim, "Multi-Space Excitation as an Alternative to the Landauer Picture for Nonequilibrium Quantum Transport," *Adv. Sci. ,* vol. 7, no. 16, p. 2001038, Aug 2020, doi: 10.1002/advs.202001038.

[11] J. Lee, H. Yeo, and Y. H. Kim, "Quasi-Fermi level splitting in nanoscale junctions from ab initio," *Proc. Natl. Acad. Sci. USA,* vol. 117, no. 19, pp. 10142-10148, May 12 2020, doi: 10.1073/pnas.1921273117.

[12] J. Lee, H. Yeo, R.-G. Lee, and Y.-H. Kim, "Ab initio theory of the nonequilibrium adsorption energy," *npj Comput. Mater.,* vol. 10, no. 1, 2024, doi: 10.1038/s41524-024-01242-5.